Electric Motor Noise from Small Quadcopters: Part II – Source Characteristics
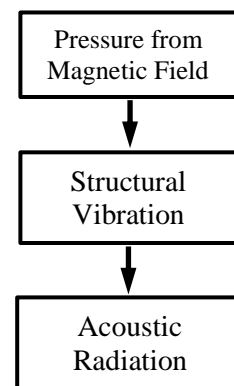
Brenda S. Henderson, Dennis Huff, Jordan Cluts, and Charles Ruggeri
NASA Glenn Research Center, Cleveland, Ohio 44135

The increased interest in electric motors for aircraft propulsion systems has driven interest in quantifying the contribution of electric motor noise to the overall sound levels and possibly human annoyance of the propulsion system. This work presents acoustic measurements of electric motors used for small quadcopters to quantify the sound produced by a number of outrunner motors with different types of controllers. Results are presented for loaded and unloaded motors as well as installed and uninstalled configurations. Motor resonance frequencies were measured and computed. Current probe measurements showed significant harmonic content in the supply current from the controllers for both the conventional and sinewave controllers. Acoustic results showed motor noise is typically radiated at frequencies near that for azimuthal vibration mode number 2 of the rotor which occurs at roughly 5000 Hz. Electric motor noise was evident in the spectra produced by many of the motor-controller combinations for motors loaded with propellers with levels often greater than those for the motor alone due to increases in the stator magnetic flux density with increased current. An installed quadcopter configuration produced increases in acoustic radiation over that of the uninstalled motor in a frequency range near the 1200 Hz azimuthal vibration mode 1 of the rotor.

I. Introduction

Small Unmanned Aircraft Systems (sUAS) flying over populated areas are becoming an increasing source of unwanted sound within communities. The number of sUAS operating in the airspace is increasing and the demand is expected to grow significantly. There are plans to use sUAS for package deliveries to residential locations[1] and visions of using larger vertical lift vehicles for transporting people for on-demand mobility in urban areas[2]. For both of these applications, it will be important to develop prediction methods that can be used to evaluate the impact of these aircraft on the community. The focus of the work reported here is to investigate the electric motor component of the noise produced by small quadcopter type sUAS. The work reported in a companion paper[3] focuses on source identification using a phased array and on directivity characteristics. In this paper (Part II), the impacts of motor type, controller type, loading, and vehicle installation on the resulting acoustic field are investigated and the frequencies of the radiated tones related to the magnetic pressure loading and subsequent motor rotor vibration. A longer term objective of this work is to develop noise prediction methods for a wide range of motor sizes that can be used in aircraft noise prediction codes such as NASA's Aircraft Noise Prediction Program (ANOPP).

Acoustic radiation from electric motors is the result of vibration of the electric motor structure[4,5]. The structural vibration is typically the result of unsteady radial loading on the stator for in-runner (external stator) motors or the rotor for outrunner (internal stator) motors by the electromagnetic field. The magnetic forces in a motor are created by a combination of electromagnets with force proportional to current and permanent magnets which exhibit an essentially predetermined force based on the motor design. The force associated with the electromagnets is impacted by the motor controller or driver as these elements in the electrical system impact the current supplied to the motor. A flowchart of the process is shown in Fig. 1. The unsteady loading can be computed from Maxwell's stress tensor and, for a linear system, is the superposition of the pressures associated with the rotor and stator fields[5,6,7,8,9,10].

Pressure from Magnetic Field

↓

Structural Vibration

↓

Acoustic Radiation

Figure 1. A flowchart for the process leading to acoustic radiation of electric motors.

Rotor eccentricity[4,11,12,13], which can be static resulting from a misalignment of the rotor and stator centerlines or dynamic resulting from shaft whirling, also contributes to unsteady radial loading. Additionally, cogging torque, the result of the interaction of the rotor magnetic field with the stator teeth, produces unsteady tangential loading on the stator teeth that can couple with the motor structure to produce acoustic radiation[14,15,16].

The structural vibrations leading to acoustic radiation of noise for in-runner motors, where the stator vibrations are important, have been reasonably well modelled[17,18]. For motors enclosed by a housing, thin shell theory has been applied to capture the structural vibrations associated with the housing[4]. For outrunner motors without an external housing (the type used in this study), the vibrations leading to acoustic radiation are those associated with the rotor. For these types of motors, some investigations have applied the stator vibration equations to the rotor[19]. Additionally, thick wall theory has been applied for the lowest azimuthal mode where the rotor sleeve and permanent magnets are treated as two thick-walled cylindrical shells[20]. For thin shell rotors, thin shell equations for rotating cylinders[21] and stringer stiffened cylinders[22] exist but the rotors investigated here fall somewhere between thin and thick shells and the magnets which are glued to the surface of the motors do not behave as stringers.

Prediction of acoustic radiation from electric motors has been approached empirically and analytically. The empirical model provides levels in octave bands and was developed from databases for much larger motors than those used here[23]. Analytical approaches[24,25,26,27] include models using a radiating infinite cylinder and models using a finite cylinder with end baffles. Computational models may also be used. For the analytical and computational approaches, the surface frequencies, modes, and vibration amplitudes must be known.

The present study investigates the impact of the motor type, controller, loading, and installation on the acoustic radiation from small quadcopter-type motors. Section II describes the experimental and computation methods. Section III reviews electromagnetic pressure loading theory. Results are presented in Section IV and include supply current waveform measurements, motor vibration measurements and calculations, and far field acoustic measurements for the unloaded, loaded motors, and installed motors. Conclusions are presented in Section V.

II. Experimental and Computational Approach

The experiments were conducted in the Acoustic Testing Laboratory (ATL) at the NASA Glenn Research Center (see Fig. 2), an anechoic chamber with a cut-off frequency of 100 Hz. The interior dimensions of the chamber are 6.4 m deep x 5.2 m wide x 5.2 m high. The ATL has removable steel grating panels suspended over the floor wedges that can be used to convert the facility into a hemi-anechoic chamber. The floor panels were found to have little impact in initial electric motor noise measurements and, therefore, were left in the chamber for all measurements reported here.

**(a)**   **(b)**
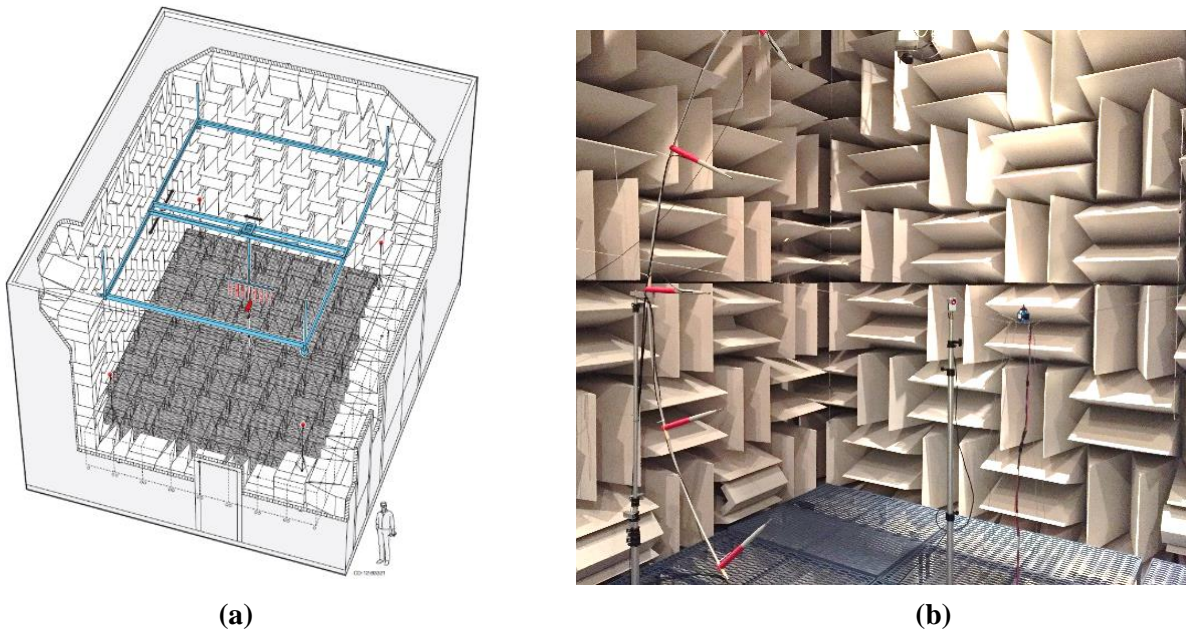
Figure 2. The Acoustic Test Laboratory at the NASA Glenn Research Center showing (a) a schematic and (b) a photograph of the chamber with the motor and microphone array.

The motors were suspended near the center of the chamber with nylon fishing line used to minimize unwanted vibrations and associated sound from the motor mount (see Fig. 3). The nylon fishing line was attached to wooden craft sticks which were mounted at the base of the motor through a vibration isolation mount. Any attempt to attach the isolation mount to a sting was found to introduce unwanted noise from the motor-sting interface. Results from phased array measurements showed that the sound source levels associated with the mount were below those of the motor.

A five element, circular-arc microphone array was located at 1 m from the outer edge of the motor casing as shown in Figs. 2 and 4. The array consisted of GRAS type 46BE free-field microphones. The sensitivity and dynamic range of the microphones were found to be sufficient for evaluating the tones produced by the motors. Acoustic measurements were acquired at a sampling rate of 200,000 Hz, are corrected for sensitivity, and are presented as narrowband sound pressure level spectra with a bandwidth of 6.1 Hz unless otherwise stated. A Hann window has been used for the Fourier transformed data. Only the data for microphone 7 are presented here as directivity studies presented in the companion paper[3] show that peak acoustic radiation occurs at an angle of 90° to the motor.
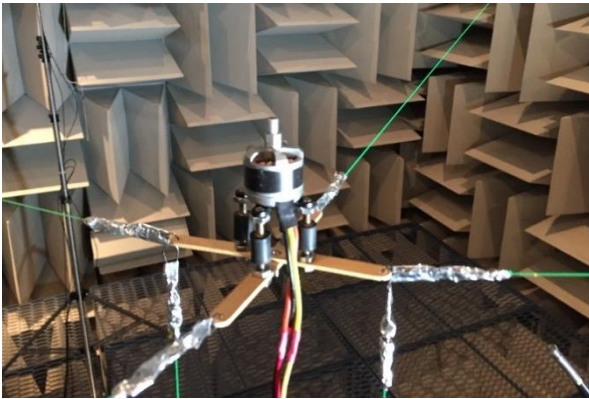
Figure 3. A photograph of the motor mount used in the experiments.
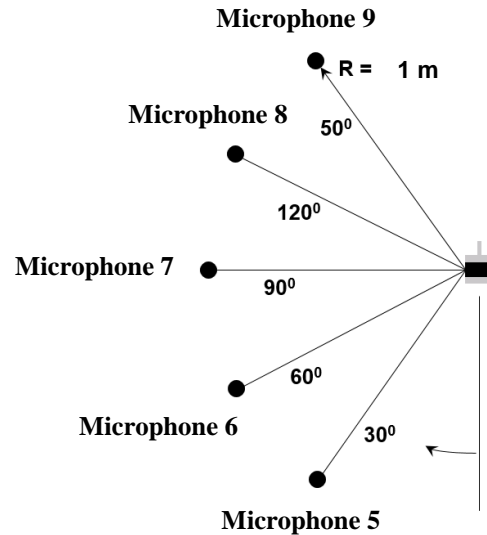
Figure 4. The microphone array used in electric motor noise experiments.

The experiments used three different types of brushless DC motors with similar characteristics (three-phase outrunner motors with 14 poles and 12 slots) and slightly different motor constants. The motor physical parameters and constants are found in Table 1. The type designation provides the stator dimensions in millimeters with the first two digits indicating the stator diameter and the last two digits the stator length. The parameters L and D are the length and outer diameter of the rotor, respectively. The motor constant, K_v, is proportional to the reciprocal of the motor torque constant and a function of the number of series conductors per coil. Increasing the number of series conductors decreases K_v. The DJI 2212 and 2312 motors have different types of conductors with the DJI 2212 using a two-strand wire and the DJI 2312 using single-strand wire with a larger diameter than that used in the DJI 2212. The DJI 2312 has a double layer winding. Most quadcopter motors

Table 1 Motor Parameters

Manufacturer	Type	K_v	L/D
DJI	2212	920	0.49
DJI	2312	960	0.49
3DR	2830	850	0.54

of the size used in this study use a delta dLRK or LRK winding scheme. The motors were controlled with three different electronic speed controllers (ESCs). Two of the controllers, the DJI E300 and the 3DR, provide a somewhat typical pulse-width modulated square wave current. The third controller, the DJI 420S (designated the sign wave controller), provides a pulse-width modulated sine-wave *like* current. The required pulse-position modulation to all ESCs was supplied by a LabVIEW program. The power to the ESCs was supplied by a benchtop DC power supply. Unless otherwise stated, data are presented for the motor alone. For the experiments with the motor loaded with a propeller, a DJI 9443 propeller was used.

The motor speeds used in the experiments are shown in Table 2. The lowest speed for the vibration studies was slightly lower than that used in the acoustic studies and was selected in an effort to isolate a vibration mode of interest (azimuthal mode 1). For the DJI 2212 motor with the sine wave controller, acoustic measurements were made at an

additional speed (4773 RPM) not used with other combinations of motors and controllers as the additional speed represented a condition where the acoustic radiation peaked.

A limited series of measurements were conducted with the DJI 2212 motors installed in a DJI Phantom 2 body as shown in Fig. 5. The body was tethered in a similar fashion to that used for the isolated motors. Only the E300 controllers were used in these experiments. The controllers and a battery were placed in the body to simulate the correct weight and weight distribution of the quadcopter components. The motors were mounted directly to the body with no isolation mounts to simulate a realistic mounting condition. While four motors were mounted in the body, the data were acquired with only one motor operating for direct comparisons of the acoustic radiation for the installed and uninstalled motors.

Figure 5. A photograph of the mount used for the installed motor experiments.

The speed of the motors was determined from a laser tachometer capable of measurements up to 250,000 RPM. The tachometer signal was recorded simultaneously with the acoustic measurements on the LabVIEW system used to supply the pulse-position modulation signal to the controllers.

Current measurements were made on one phase supplied to the motor using a Tektronix TCP-303 current probe and were recorded on the LabVIEW acquisition system. The current measurements had to be made separately from the acoustic measurements since the sinewave controllers required very short wire lengths between the controller and motor which placed the current probe very close to the motor where it served as an unwanted reflective surface.

The static (open circuit) resonance frequencies and mode shapes of the motors were determined by hanging the motor or rotor from a string, supplying an initial impulsive excitation to the rotor, and measuring the resulting vibration at two different locations on the rotor using PCB 352C23 accelerometers. One of the accelerometers remained in the same location while the other accelerometer was moved to different circumference locations on the rotor to ascertain mode shape. The combined weight of the accelerometers was 1/50 the weight of the DJI 2212 rotor. The weights of all motor rotors were similar. Due to concerns with mass-loading the rotor with the accelerometers, preliminary measurements were made with a single accelerometer and these measurements produced frequencies similar to those with two accelerometers. For the DJI 2212 motors, measurements were made with isolated rotors and with the entire motor. For the DJI 2312 and 3DR motors, measurements were only made with the entire motor as results for the DJI 2212 motor indicated that the resonance frequencies for the motor and the isolated rotor were similar.

A Polytec OFV-5000 laser vibrometer with a DD-100 displacement decoder was used to measure the vibration frequencies and amplitudes of the rotating motor. To eliminate extraneous vibrations, the motor was mounted on an aluminum-extrusion frame located on an optics table. Accurate alignment of the laser to the tangent point of the motor shell was accomplished with a traversing system. The laser was pointed near the bottom edge of the rotor where vibration amplitudes were expected to be the highest. Due to the small amplitude vibrations of the rotor, the vibrometer was set to 2 microns/V, its maximum sensitivity. The signal from the laser vibrometer was high-pass filtered to isolate displacements associated with individual oscillation modes when multiple modes were present.

The motor speeds used in the experiments are shown in Table 2. The lowest speed for the vibration studies was slightly lower than that used in the acoustic studies and was selected in an effort to isolate a vibration mode of interest (azimuthal mode 1). For the DJI 2212 motor with the sine wave controller, acoustic measurements were made at an additional speed (4773 RPM) not used with other combinations of motors and controllers as the additional speed represented a condition where the acoustic radiation peaked.

The experimental vibration results for the DJI 2212 motor were compared to those obtained from

Table 2 Motor Conditions Used in Experiments

	4350 (RPM)	4380 (RPM)	4773 (RPM)	5370 (RPM)	6260 (RPM)
Vibration Studies	X			X	
Acoustic Studies		X	X *	X	X
*Only with DJI 2212 and the sine wave controller					

a finite element analysis performed with SolidWorks on a model that included the rotor, permanent magnets, and shaft. The stator was not included in the assembly. The magnets were attached to the rotor with a simulated epoxy resin bond to match the actual construction. It was also desirable to compare the SolidWorks simulation to a known case. As such, a thin shell model was created for which published analytical and finite element computational results exist (including modes and frequencies). For both models, the automatic meshing feature within SolidWorks was used. For the test case, the SolidWorks simulation captured modes and frequencies that were comparable to those from the analytical model and from ANSYS and Nastran published results.

III. Electromagnetic Pressure

The force due to the electromagnetic field applied to the inner surface of the outer shell of the motor (in this case the rotor) is given by[5-10]

$$F_r = \int p_r \, dA,$$

where F_r is the radial force and p_r is the radial component of the magnetic pressure. The magnetic pressures is given by Maxwell's stress tensor as

$$p_r(\alpha, t) = \frac{1}{2\mu_o}[B_r^2(\alpha, t) + B_t^2(\alpha, t)] \approx \frac{B_r^2(\alpha, t)}{2\mu_o},$$

where B is the magnetic flux density, μ_o is the magnetic permeability of free space, subscript r indicates the radial direction, subscript t indicates the tangential direction, and α is the angle relative to a coordinate system attached to the stator. The tangential component of the magnetic flux density is much smaller than the radial component and can be ignored. For a linear system, the radial component of the magnetic flux density is the superposition of the field produced by the rotor permanent magnets and the stator electromagnets and may be expressed as

$$B_r(\alpha, t) = B_{rot}(\alpha, t) + B_{stat}(\alpha, t), \tag{1}$$

where the subscripts *rot* and *stat* indicate the fields due to the rotor magnets and the stator windings, respectively.

The magnetic flux density can be computed from the product of the magnetomotive force (MMF) and the air gap permeance, λ, which includes the effect of the stator slots. The magnetic flux density associated with the permanent magnets is given by

$$B_{rot}(\alpha, t) = \sum_{n=1,3,5,\dots} B_n \lambda_o \cos[nN(\omega_{mot}t - \alpha) + \phi_n] + \sum_{n=1,3,5,\dots} \sum_k B_n \widetilde{\lambda_k} \cos[nN(\omega_{mot}t - \alpha) \pm kZ_s + \phi_n], \tag{2}$$

where the coefficients B_n are functions of the Fourier mode number, the number of pole pairs (N), the inner radius of the rotor shell, the outer radius of the stator, the depth of the magnets, the air gap depth, the magnet relative recoil permeability, and the magnet remanence, respectively. The angle ϕ_n is the phase shift between the rotor and stator harmonics. The quantities λ_o and $\widetilde{\lambda_k}$ are the average air gap permeance and the coefficient of the kth permeance mode, respectively. The permeance coefficients are functions of the Carter factor. The number of slots is given by Z_s. The motor angular speed is ω_{mot} in rad/sec. The magnetic flux density for the stator is given by

$$B_{stat}(\alpha, t) = \sum_v \sum_u b_v I_u \cos(uN\omega_{mot}t - vN\alpha + \theta_u), \tag{3}$$

where I_μ is the amplitude of the uth current mode, θ_u is the current harmonic phase shift. The coefficients b_v are functions of the Fourier mode number, effective air gap depth, coil span, rotor radius, stator radius, winding turns, and slot opening.

Combining Eqn. (1), (2), and (3) results in the radial component of magnetic flux density given by

$$B_r(\alpha, t) = \sum_{n=1,3,5,\dots} B_n \lambda_o \cos[nN(\omega_{mot}t - \alpha) + \phi_n] + \sum_{n=1,3,5,\dots} \sum_k B_n \widetilde{\lambda_k} \cos[nN(\omega_{mot}t - \alpha) \pm kZ_s\alpha + \phi_n] + \sum_v \sum_u b_v I_u \cos(uN\omega_{mot}t - vN\alpha + \theta_u),$$

where the first two terms on the right hand side are associated with the rotor magnets and the last term is associated with the stator winding field. The radial magnetic pressures is, therefore, given by

$$p_r(\alpha, t)$$

$$= \frac{1}{4\mu_o}\left\{\sum_n \sum_m B_n B_m \lambda_o^2 \cos[(n \pm m)N(\omega_{mot}t - \alpha) + \phi_n \pm \phi_m]\right.$$

$$+ \sum_n \sum_k \sum_m \sum_j B_n B_m \widetilde{\lambda_k}\widetilde{\lambda_j} cos[(n \pm m)N(\omega_{mot}t - \alpha) \pm (k \pm j)Z_s\alpha + (\phi_n \pm \phi_m)]$$

$$+ \sum_v \sum_u \sum_\eta \sum_w b_v b_\eta I_u I_w cos[(u \pm w)N\omega_{mot}t \mp (v + \eta)N\alpha + (\theta_u \pm \theta_\eta)]$$

$$+ 2\sum_n \sum_m \sum_k B_n B_m \lambda_o \widetilde{\lambda_k} \cos[(n \pm m)N(\omega_{mot}t - \alpha) \pm mkZ_s\alpha + (\phi_n \pm \phi_m)]$$

$$+ 2\sum_n \sum_v \sum_u B_n \lambda_o b_v I_u \cos[(n \pm u)N\omega_{mot}t - N(n \pm v)\alpha + (\phi_n \pm \theta_u)]$$

$$+ 2\left.\sum_n \sum_k \sum_v \sum_u B_n \widetilde{\lambda_k} b_v I_u cos[(n \pm u)(N\omega_{mot}t) - (n \pm v)N\alpha \pm kZ_s\alpha + (\phi_n \pm \theta_u)]\right\}.$$

.
$$(4)$$

Table 3 Electromagnetic Frequencies and Modes

Equation 4 Term	Frequency (Hz)	Mode
1	$(n \pm m)Nf_{mot}$	$(n \pm m)N$
2	$(n \pm m)Nf_{mot}$	$(k \pm j)Z_s \pm (n \pm m)N$
3	$(u \pm w)Nf_{mot}$	$(v \pm \eta)N$
4	$(n \pm m)Nf_{mot}$	$(n \pm m)N \pm mkZ_s$
5	$(n \pm u)Nf_{mot}$	$(n \pm v)N$
6	$(n \pm u)Nf_{mot}$	$(n \pm v)N \pm kZ_s$

The first, second, and fourth terms on the right-hand side of Eqn. (4) are associated with the rotor field. The third term is associated with the stator field. The remaining terms are rotor-stator interaction terms. The equation above leads to the frequencies and modes shown in Table 3, where $f_{mot} = \omega_{mot}/2\pi$ and f_{mot} is the motor speed in Hz. The integers u and w are associated with the current and, therefore, can only take on values associated with the fundamental line frequency harmonics present in the motor supply current (see Section IV A for further discussion). Integers n and m are associated with the harmonics of the permanent magnet field and only assume odd values. Integers k and j are associated with the airgap permeance space harmonics. Integers v and η are associated with the space harmonics of the stator magnetic flux density. The magnitude of the stator term (term 3) is proportional to the square of the current mode amplitude when $u = w$. For the rotor-stator interaction terms, the magnitude is proportional to the current mode amplitude. All frequencies are equal to integer multiples of the motor speed and, therefore, the fundamental line frequency of the supply current given by $f_l = f_{mot}N$, where N is the number of pole pairs. All motors used in this study have seven pole pairs.

In addition to the frequencies in Table 3, dynamic rotor eccentricity (whirling of the rotor shaft) can result in frequency side lobes in the acoustic and vibration spectra[4,11,12]. The eccentricity impacts the permeance, λ, of the airgap due to the non-uniform orbit of the rotor and, therefore, impacts the magnetic field. The side lobes have frequencies equal to those in Table 3 $\pm qf_l/N$, where q is an integer. In addition to shaft whirling, static misalignment of the rotor shaft relative to the stator core affects the permeance and magnetic field but does not create frequency side lobes in the vibration spectra.

IV. Results

The results from the current probe measurements are presented first followed by the motor vibration studies, far-field acoustics, and finally installed acoustic results. As discussed in the previous section, the current supplied to the motor impacts the stator magnetic flux density and, therefore, impacts the unsteady rotor loading for loading associated with the stator field or the rotor-stator interactions. Understanding rotor natural frequencies is important as pressure loading at frequencies near a natural frequency of the rotor will result in relatively large displacements and significant acoustic radiation. The greater the harmonic content of the current supplied to the motor, the more likely one of the harmonics will produce loading at a frequency close to a natural frequency of the rotor.

A. Electromagnetic Loading - Current Probe Results

Results from current probe measurements with the E300 controller and two different motors are shown in Fig. 6 (a) for a motor speed of 5370 RPM. The data have been phased shifted for clarity. Superimposed on Fig. 6 (a) is the expected voltage supplied by a six-step brushless DC (BLDC) motor drive where the pulse-width modulation has been omitted for clarity. For both motors, the current supplied to the motors is not purely a pulse-width modulated square wave and, therefore, is expected to contain harmonics other than those typically observed for six-step BLDC drives. The current appears to overshoot when switching from zero current to the high state and when switching from the high state to zero current. The maximum current amplitude for the 3DR motor is slightly greater than that for the DJI 2212 and slightly lower than that for the DJI 2312 (not shown in the Figure).

The current-probe data for the DJI 2212 motor with the E300 and 3DR conventional controllers are shown in Fig. 6 (b) for a motor speed of 5370 RPM. The waveform characteristics for both controllers are similar although the pulse-width modulation frequency is lower for the 3DR controller (roughly 16.5 kHz) than for the E300 controller (roughly 27.5 kHz). Data acquired with these two controllers for the 3DR motor showed results similar to those in Fig. 6 (b). The maximum current levels for the 3DR controller are slightly higher than those for the E300 controller.
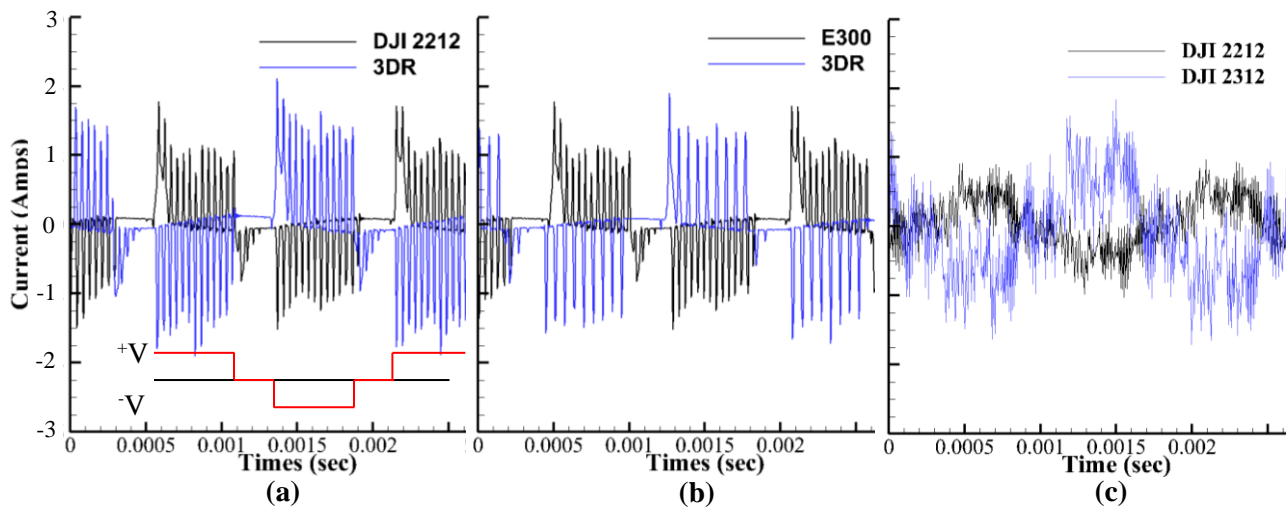
Figure 6. Current probe signals for (a) the DJI 2212 and 3DR motors with the E300 controller, (b) the DJI 2212 motor with the E300 and 3DR controllers, and (c) the DJI 2212 and DJI 2312 motors and the sinewave controller. For all cases, the motor speed was 5370 RPM.

Current probe results for the DJI 2212 and DJI 2312 motors with the sine wave controller at a motor speed of 5370 RPM are shown in Fig. 6 (c). The sine wave controller produces a sine wave *like* current which is not a pure sinewave and, therefore, will have an associated spectrum rich in harmonics. The amplitude of the current for the DJI 2312 is slightly higher than that for the DJI 2212. The pulse width modulation appears to be at a much higher frequency for the sine wave controller than for the conventional controllers.

The spectra obtained from the current probe measurements with the E300, 3DR, and sine wave controllers are shown in Fig. 7 for the DJI 2212 motor. The data for 5370 RPM have been offset by 10 dB and for 6260 RPM by 20 dB for clarity. For each motor speed, the fundamental line frequency and its harmonics are indicated by square data symbols. All controllers result in current spectra with harmonics of significant amplitude although the amplitude of the fundamental is 10 – 20 dB greater than any harmonic. The amplitudes of the fundamental line frequency change little with speed for the conventional controllers and increase slightly with speed for the sine wave controller. The effect of pulse-width modulation is not observed in the spectra of Fig. 7 due to the relatively high modulation frequencies.
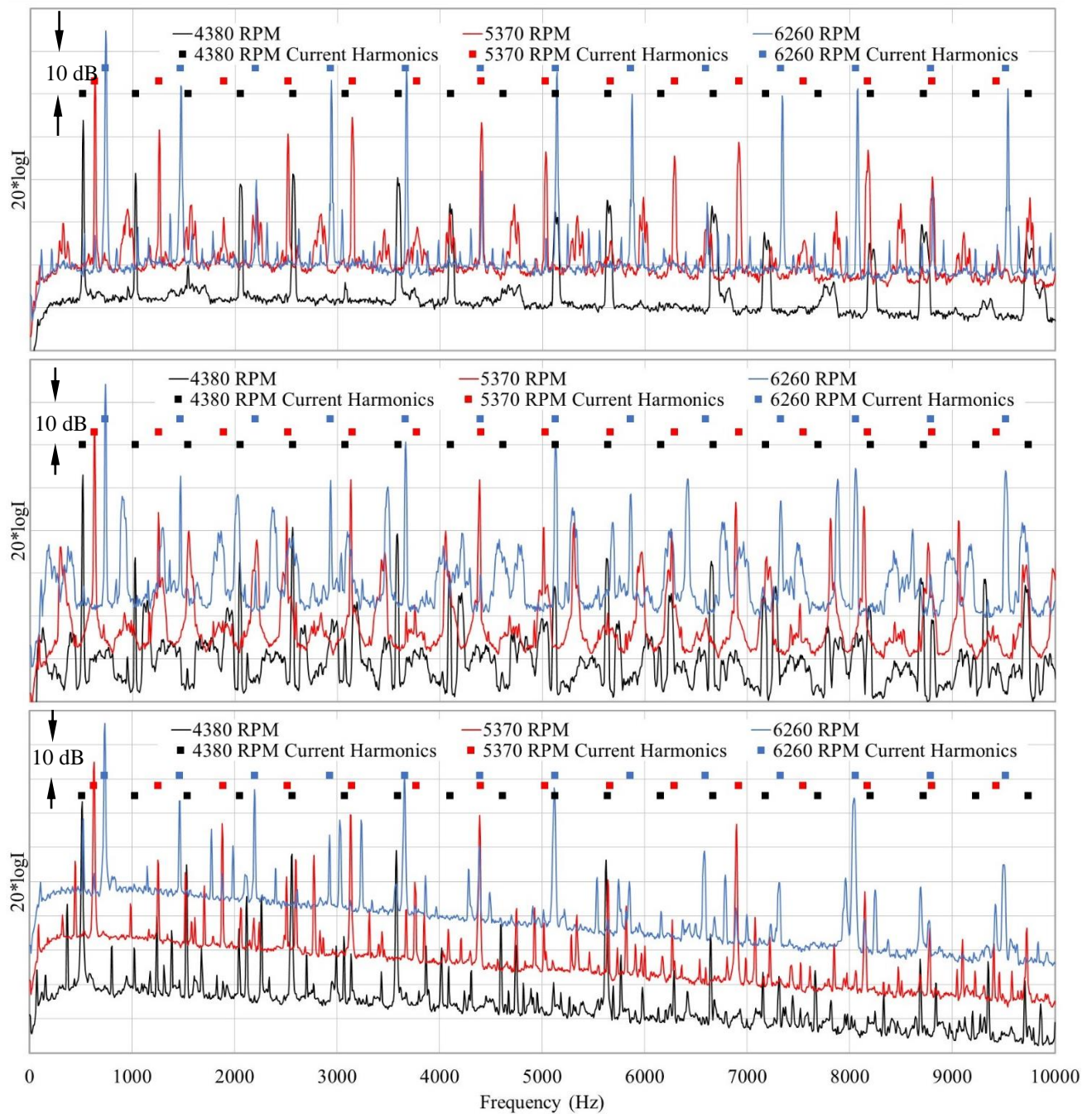
Figure 7. Spectra obtained from the current probe measurements with the DJI 2212 motor and the E300 (top), 3DR (middle), and sine wave (bottom) controllers. The data for 5370 RPM and 6260 RPM have been offset by 10 dB and 20 dB, respectively. The fundamental line harmonics are marked for reference.

For the DJI 2212 motor with the E300 controller and a motor speed of 4380 RPM [see Fig. 7 (top)], all harmonics other than those at multiples of the third harmonic (triplen and non-triplen) are present in the spectra with amplitudes that are greater than 20 dB above the broadband for frequencies up to 7000 Hz. At a motor speed of 5370 RPM, small amplitude discrete peaks begin to appear for multiples of the third harmonic and discrete peaks appear 10 – 15 dB above the broadband for odd harmonics of a peak near 320 Hz, a frequency unrelated to the fundamental line frequency. The harmonic content of the current signals at the highest and lowest motor speeds are similar except for the addition of low amplitude secondary discrete frequencies that are not related to the fundamental line frequency appearing at the highest motor speed.

The spectra associated with the DJI 2212 motor and the 3DR conventional controller [see Fig. 7 (middle)] contain all harmonics of the fundamental line frequency other than those at multiples of the third harmonic as well as many other discrete frequency peaks that are not harmonically related to the fundamental line frequency for all motor speeds investigated. Far more discrete peaks appear in the spectra associated with the 3DR controller than the E300 controller.

For the sine wave controller [see Fig. 7 (bottom)], the largest amplitudes in the current signal occur for the 1, 3, 5, and 7 harmonics of the fundamental line frequency at all motor speeds. The amplitudes of the fundamental line frequencies are roughly 3 dB lower than those for the E300 controller. All motor speeds result in a secondary fundamental current component at a fundamental frequency equal to roughly 70% of the fundamental line frequency. Other discrete frequency peaks not harmonically related to the fundamental line frequency or the secondary fundamental frequency are also observed in the spectra.

Results from current probe measurements with the DJI 2212 motor using the E300 controller are shown in Fig. 8 (a) for the motor alone and for the motor loaded with propeller. The data were acquired at a motor speed of 5370 RPM. The current spectra at multiple speeds are presented in Fig. 9. The time traces show the waveforms are slightly different for the motor and the motor loaded with the propeller. For all motor speeds, the motor alone and the motor loaded with the propeller show similar frequency content with an increase in the amplitudes of the 1, 5, 7, and 11 harmonics for the motor + propeller case relative to the motor alone.
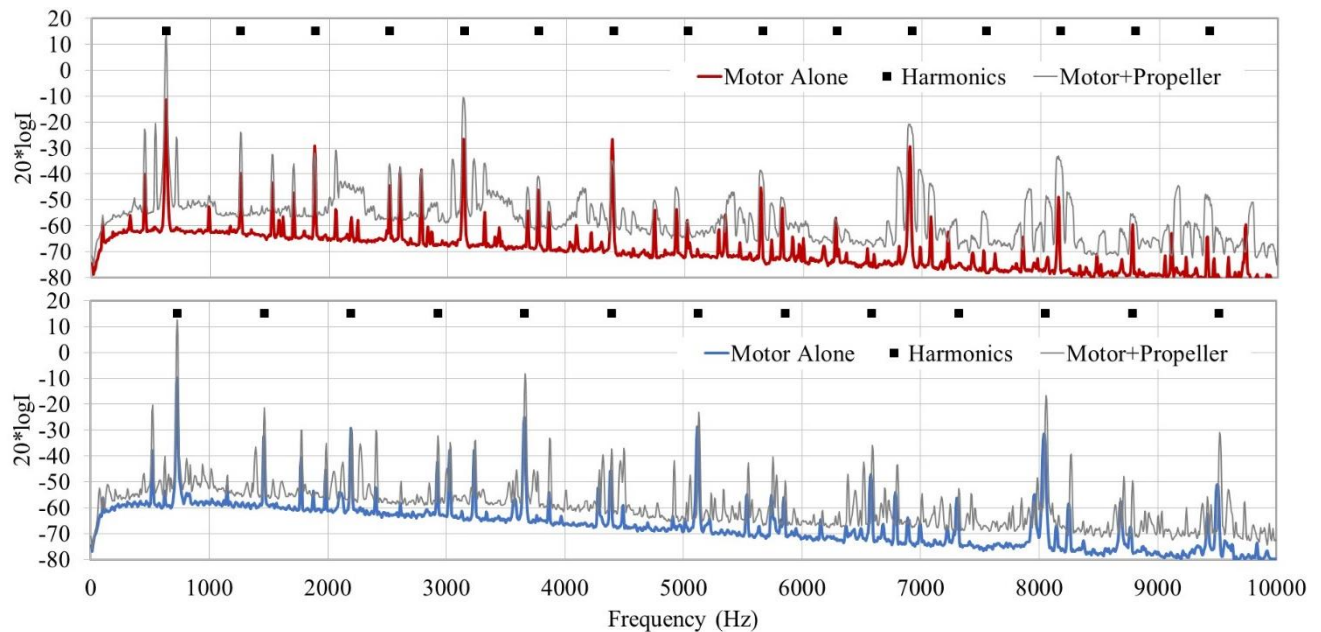
Results from current probe measurements with the DJI 2212 motor using the sine wave controller are shown in Fig. 8 (b) for the motor alone and for the motor loaded with a propeller. The motor speed is the same as that used in Figs. 8 (a) and 9. The data have been phase shifted for clarity. The current spectra for two motor speeds are shown in Fig. 10. The amplitudes of the 1, 5, and 11 harmonics are increased with loading over those associated with the motor alone. For both motor speeds, additional discrete frequencies appear in the spectra for the motor + propeller that were not present in the spectra for the unloaded motor.
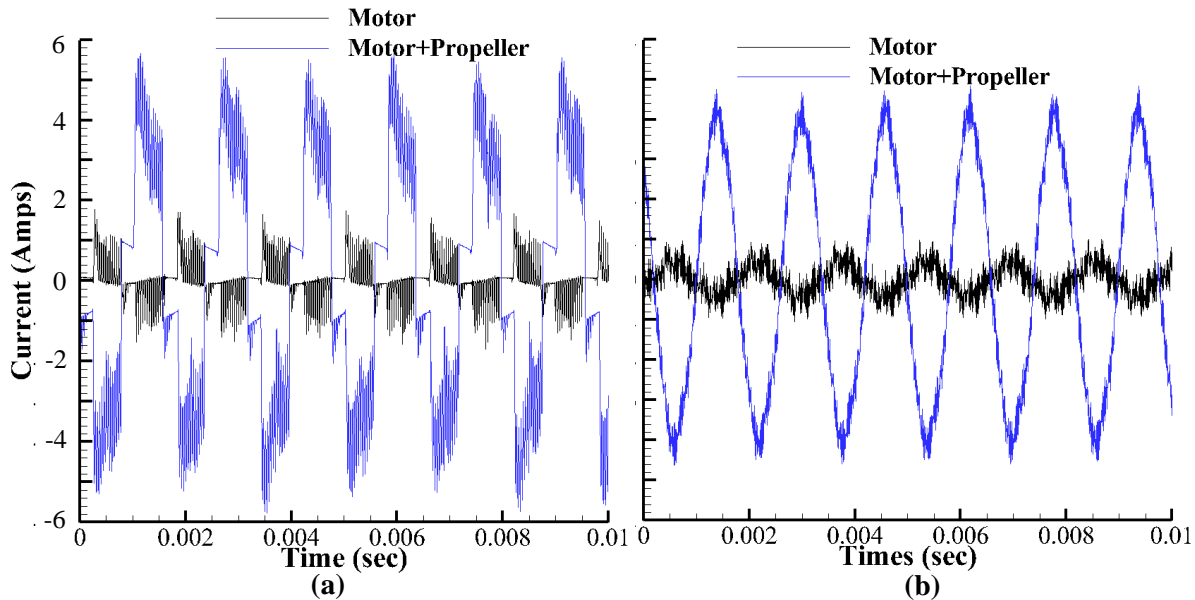
Figure 8. Current probe signals for the DJI 2212 motor at 5370 RPM using the (a) E300 and (b) sine wave controllers.
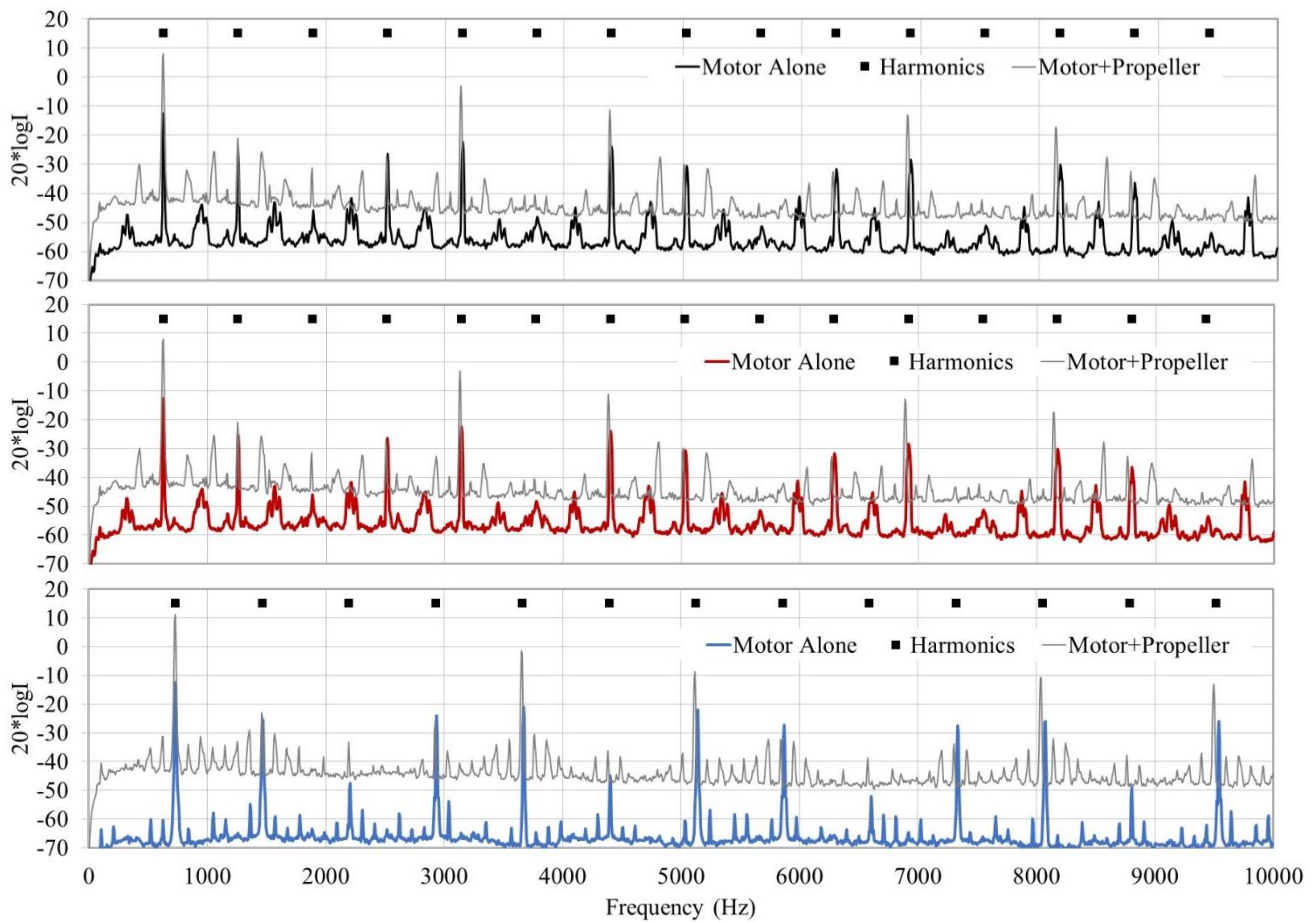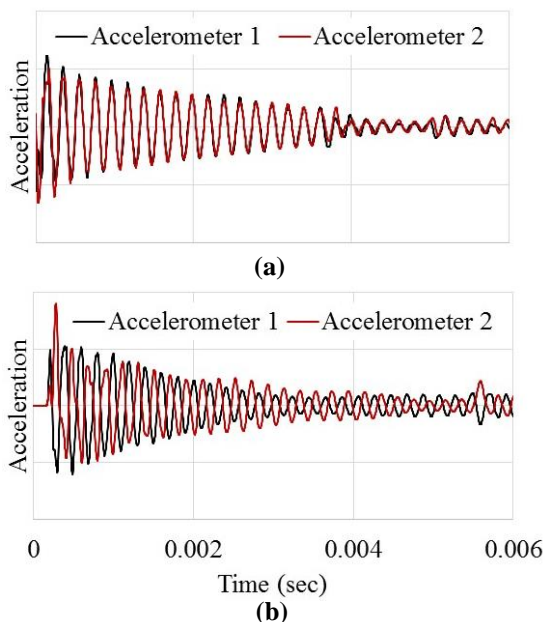
Figure 9. Spectra obtained from the current probe measurements with the DJI 2212 motor alone and loaded with a propeller for motor speeds equal to 4380 (top), 5370 RPM (middle) and 6260 RPM (bottom). The data were obtained with the E300 controller. The fundamental line harmonics are marked for reference.

Figure 10. Spectra obtained from the current probe measurements with the DJI 2212 motor alone and loaded with a propeller for motor speeds equal to 5370 RPM (top) and 6260 RPM (bottom). The data were obtained with the sine wave controller. The symbols mark the harmonics of the fundamental line frequency.

B. Motor Vibration

Sample results for the open-circuit vibration tests on the DJI 2212 rotor are shown in Fig. 11 for in-phase and out-of-phase accelerometer signals. The frequencies obtained from the measurements on the DJI 2212, DJI 2312, and 3DR motors are shown in Table 4. Two different DJI 2212 motors, designated (1) and (2) in Table 4, were included in the study. For one DJI 2212 motor, data were acquired on the rotor alone as well as the entire motor (rotor with stator). The results show that the resonance frequency for the motor is slightly higher than that for the rotor alone. Resonance frequencies are similar ($\pm$0.2%) for different samples of the same type of motor. The resonance frequencies of the DJI 2212 motor are slightly lower than that of the DJI 2312 motor and slightly higher than that of the 3DR motor.

The mode shape determined from the measurements on the DJI 2212 motor is shown in Fig. 12 for the frequencies in Table 4. For the deflection shape shown, accelerometers 1 and 2 are in phase and 1 and 2' out of phase. The mode shape for the rotor alone and for the motor (rotor + stator) were the same. The mode shape is consistent with azimuthal mode 2.

The waveform obtained from a simulation of the time series that would be obtained from laser vibrometer measurements on a rotating cylinder oscillating in azimuthal modes 1 and 2 are shown in Figs. 13 (a) and (b), respectively. The motor speed for Fig. 13(a) was 4350 RPM and for Fig. 13 (b), 5370 RPM. The amplitudes of modes 1 and 2 were 5 μm and 0.5 μm, respectively. For azimuthal mode 1, the motor rotation period (indicated by red lines in Fig. 13), envelopes the time series of the displacement and the shorter period within the motor rotation envelope is equal to the period of azimuthal mode 1. The amplitude of the envelope is equal to the displacement amplitude of azimuthal mode 1. For azimuthal mode 2, a period of ½ the motor rotation period envelopes the time series (designated 2* Motor Rotation).

Results from the vibrometer measurements for the DJI 2212 motor with the E300 controller are shown in Figs. 14 (a) and


(a)

(b)

Figure 11. The accelerometer time traces for the 2212 DJI rotor showing (a) in-phase and (b) out-of-phase responses of the structure.

Table 4 Measured Resonance Frequencies

Motor	Rotor Frequency (Hz)	Motor Frequency (Hz)
DJI 2212 (1)	4900	5000
DJI 2212 (2)		5010
DJI 2312		5060
3DR		4460

(b) for two different motor speeds. For the lower motor speed, only the frequency for azimuthal mode 1 was observed in the spectra (not shown here). At the higher motor speed, frequencies for the first and second modes were observed and the results shown in Fig. 14 (b) are for a signal that was high-pass filtered to eliminate the mode 1 contribution. The amplitudes of the vibrations for mode 1 and 2 are roughly 5 μm and 1/2 μm, respectively. The frequencies for mode 1 and 2 at the indicated motor speeds are 1025 Hz and 4600 Hz, respectively. The frequencies and amplitudes of the forced response of the rotor will change with motor speed as the rotor vibrations are a function of the applied electromagnetic force and the frequency response of the rotor. However, results from the experiments and the finite element analysis that follows show the frequencies obtained from the vibrometer measurements are close to the rotor resonance frequencies.

Results from the finite element analysis of the open-circuit (static) motor are found in Fig. 15 and summarized for a number of configurations in Table 5. As stated previously, only the rotor was modelled as the experimental results indicated the resonance frequencies for the rotor and motor (rotor + stator) were similar. All entries in Table 5 are for free vibration of the rotor structure. The analysis was performed with and without a thin layer of adhesive between the magnets and the rotor to determine the impact of the adhesive as a variation in the adhesive layer may occur between different samples of the same type of motor. An adhesive layer was used for all rotating configurations in Table 5. The results in Fig. 15 show that the lower and higher frequencies in Table 4 correspond with azimuthal modes 1 and 2, respectively. However, it should be noted that the end bell of the rotor affects the vibration mode and the rotor shell is not vibrating as a simple shell. This is expected to impact attempts to predict rotor vibrations with analytical methods and acoustic radiation with simple cylindrical shell models. The results for azimuthal mode 2 of the static rotor are close to those obtained from the experiments. The adhesive layer impacts the mode 2 resonance frequency. Rotation increases the resonance frequency for mode 1 and decreases the resonance frequency for mode 2. Frequencies predicted by thin shell theory (not included here) did not match those from the finite element analysis or the experimental measurements.
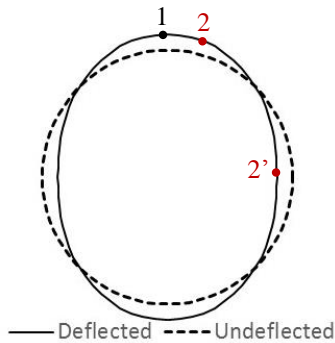

Figure 12. The mode shape of the 5000 Hz resonance frequency determined experimentally for the DJI 2212 rotor.

(a)

(b)
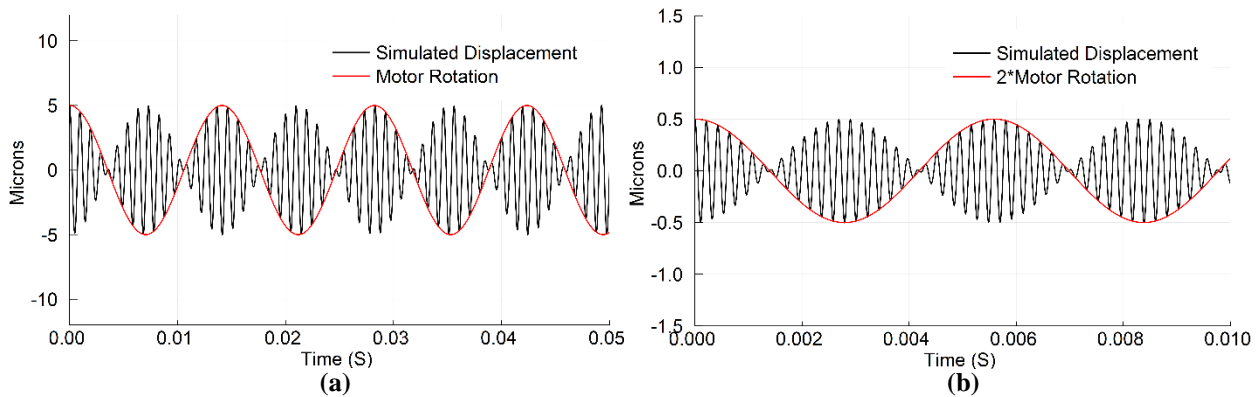
Figure 13. Simulated displacements of a rotating surface for a spatially fixed angular location. The results are for (a) azimuthal mode 1 with a surface rotation speed of 4350 RPM and (b) azimuthal mode 2 with a surface rotation speed of 5370 RPM.

12
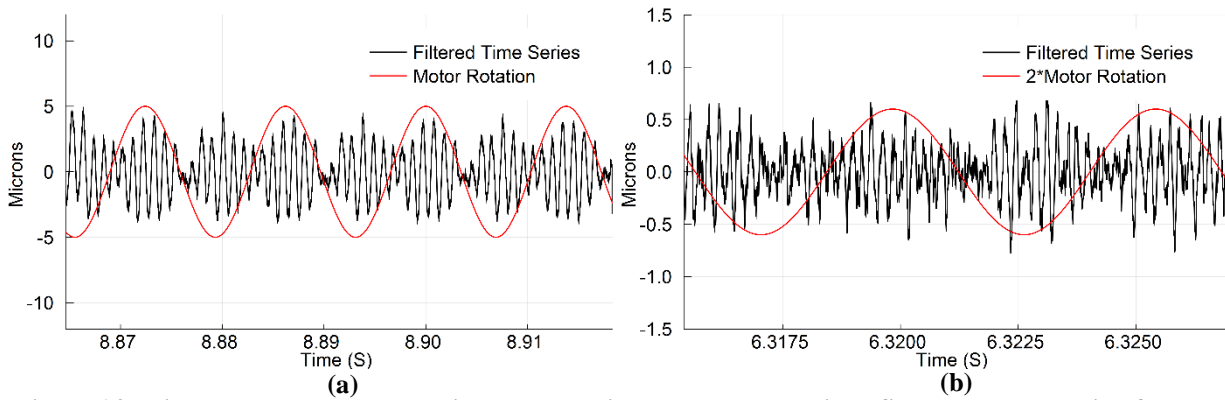
Figure 14. Displacements measured with the laser vibrometer at a spatially fixed angular location for motors speed equal to (a) 4350 RPM and (b) 5370 RPM. The data in (b) have been high-pass filtered to eliminate the impact of azimuthal mode 1.


| (a) | (b) | (c) | (d) |
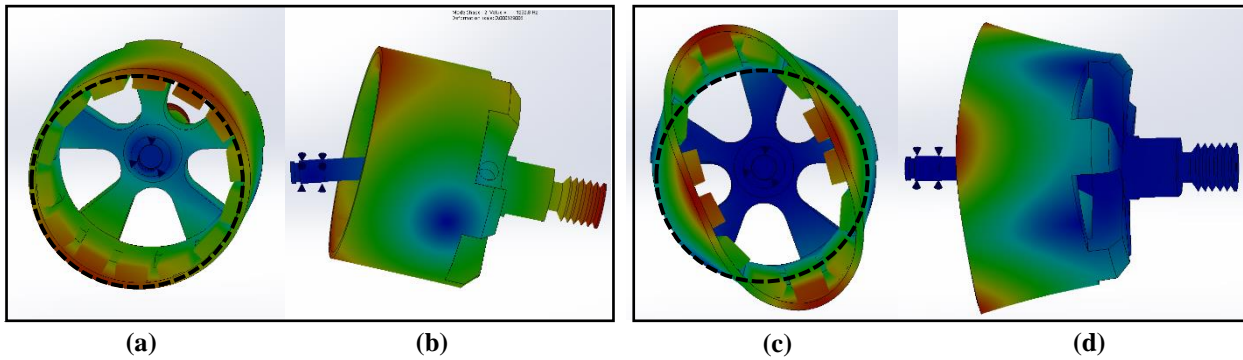
Figure 15. The deflection shapes at one point in the oscillation cycles obtained from the finite element analysis of the DJI 2212 rotor. Front views are shown in (a) and (c) and side views in (b) and (d). Results in (a) and (b) are for azimuthal mode 1 and in (c) and (d) for the azimuthal mode 2. The dashed line indicates the undeflected shape of the rotor at the axial location opposite to that of the end bell.

Table 5 Resonance Frequencies from FEA Analysis for the DJI 2212 Rotor

| Configuration	Frequency (Hz) Mode 1	Frequency (Hz) Mode 2
Static Rotor with Adhesive	1230	5020
Static Rotor without Adhesive	1230	5270
Rotor at 4350 RPM	1390	4650
Rotor at 5370 RPM	1390	4650

13

C. Acoustics

Acoustic results for the DJI 2312 motor with the E300 controller are shown in Fig. 16. Also included in the Figure are the corresponding current data and the frequency of the discrete peaks as a function of the fundamental line frequency. The current frequency labeled f_a is unexpected and not harmonically related to the fundamental line frequency. Peaks identified by an "e" are associated with rotor eccentricity as described in Section III. Multiple tones near 4500 Hz appear in the spectra for the 4380 RPM and 5370 RPM motor speeds. The frequencies of these tones are close to the mode 2 resonance frequencies predicted in Table 4. The largest amplitude acoustic tones occur for 5370 RPM. At 6260 RPM, acoustic radiation near 4500 Hz would be associated with $6*f_l$ which can be associated with the stator field third and sixth fundamental line frequency harmonics. The third and sixth current harmonics have
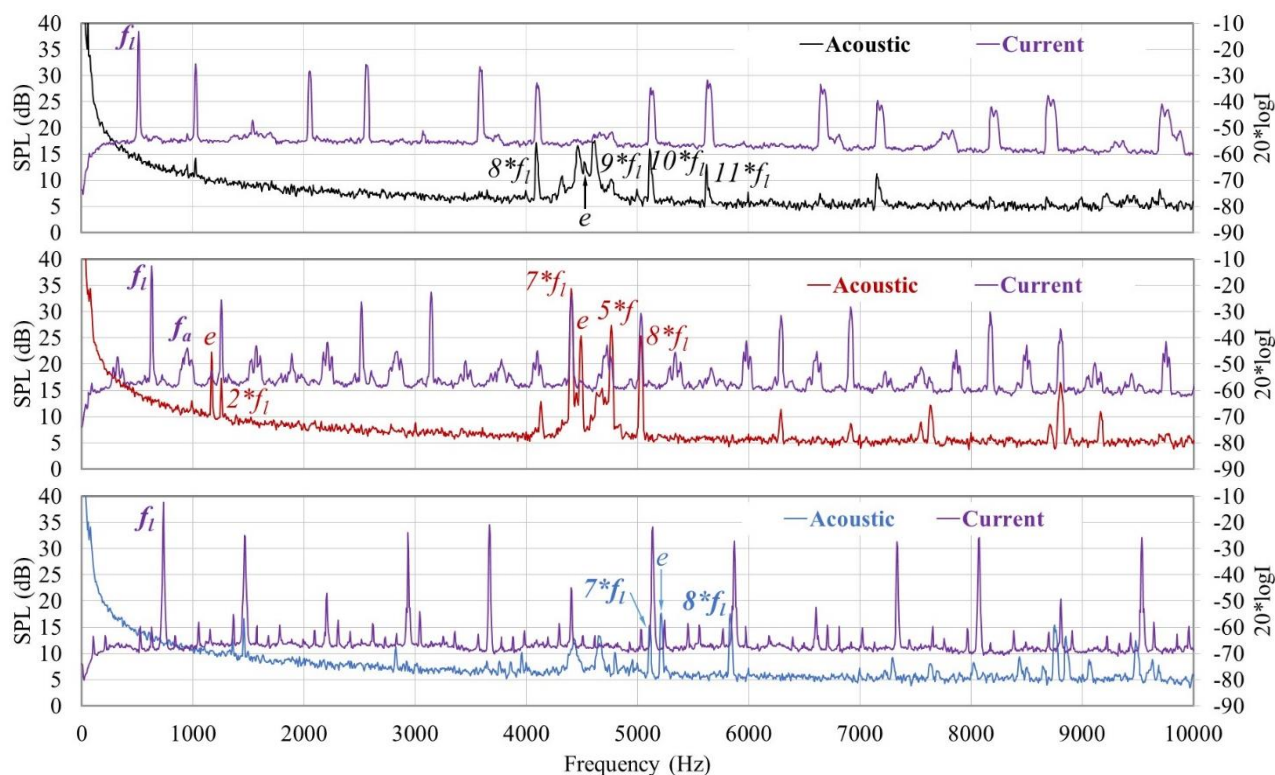
Figure 16. The acoustic data acquired for the DJI 2212 motor with the E300 controller. The data are for motor speeds equal to 4380 RPM (top), 5370 RPM (middle), and 6260 RPM (bottom). The eccentricity frequency, e, the unexpected additional frequencies, f_a, and harmonics of the fundamental line frequency, f_l, are marked for reference.

low current amplitudes which is likely the reason for the lack of acoustic radiation near this frequency. For 5370 RPM, tones are also present at frequencies near the azimuthal vibration mode 1 at roughly 1200 Hz.

The data acquired with the 3DR motor and the E300 controller are presented in Fig. 17. For all motor speeds, tones appear at frequencies near the second rotor vibration mode. The peak amplitudes occur for a motor speed of 5370 RPM and slightly exceed those for the DJI 2212 motor. Some of the large amplitude tones for 5270 RPM and 6260 RPM are not associated with integer multiples of the fundamental line frequency or with motor eccentricity frequencies. These tones may be associated with current frequencies not related to the fundamental line frequency or due to vibrations not associated with those described in Section III. The increased amplitudes of the peak tones at 4380 RPM and 6260 RPM for the 3DR motor over those for the DJI 2212 motor are likely due to the lower K_v rating of the 3DR motor which is associated with a greater number of stator winding turns. Increasing the motor turns results in a larger stator magnetic flux density.
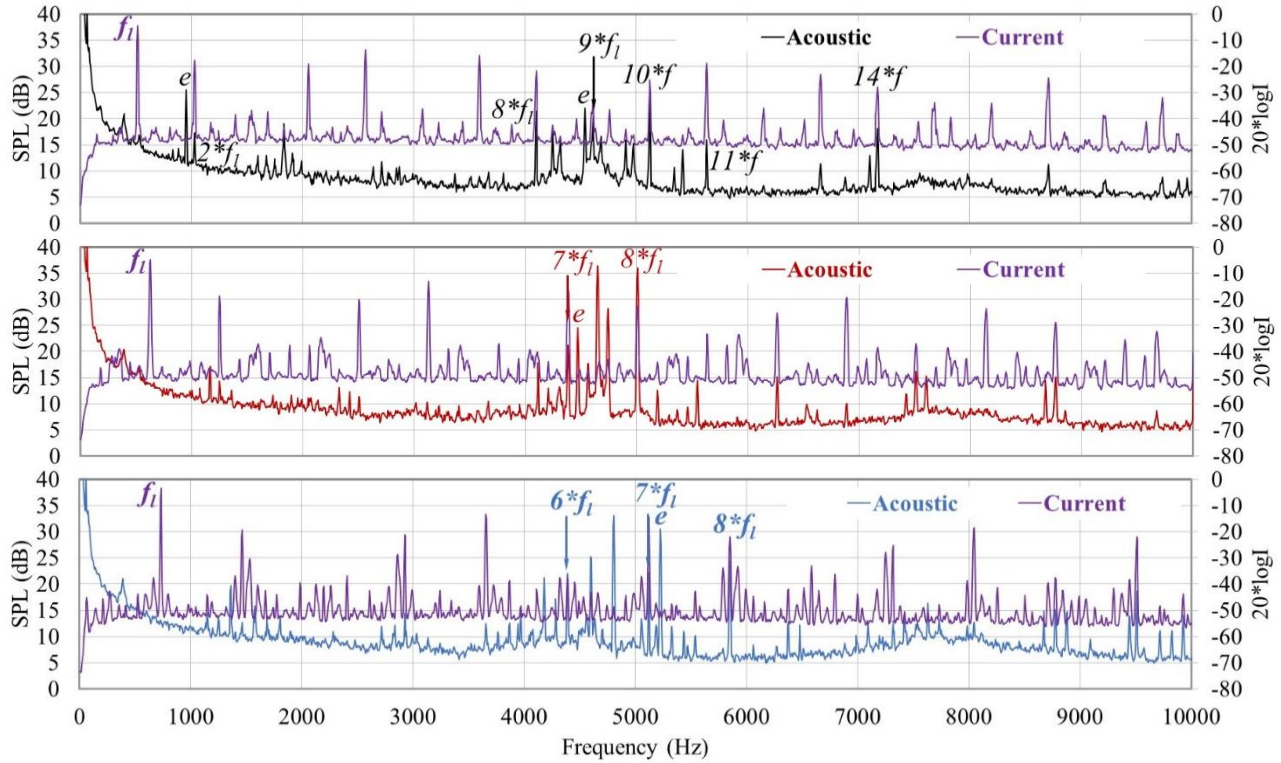
Figure 17. The acoustic data acquired for the 3DR motor with the E300 controller. The data are for motor speeds equal to 4380 RPM (top), 5370 RPM (middle), and 6260 RPM (bottom). The eccentricity frequency, e, and harmonics of the fundamental line frequency, f_l, are marked for reference.

The results for the DJI 2312 motor with the E300 controller are found in Fig. 18. Significant acoustic radiation occurs for all motor speeds near the second vibration mode frequency around 5000 Hz. The results in the previous section indicated the mode 2 frequency was slightly higher for the DJI 2312 motor than for the DJI 2212 motor which may explain the increase in the acoustic amplitudes for the DJI 2312 motor relative to the DJI 2212 motor at $7*f_l$ for 6260 RPM and $8*f_l$ at 5370 RPM. Additionally, motor eccentricities significantly contribute to the acoustic radiation at 6260 RPM. Peak radiation at a motor speed of 5370 RPM occurs at a frequency associated with $12*f_l$ and is likely associated with higher vibration modes than those investigated in Section IV B. The peak amplitudes of the tones at 4380 RPM are greater for the DJI 2312 motor than for the DJI 2212 motor.

The results for the DJI 2212 motor and the sine wave controller are shown in Fig. 19. Motors speeds of 4380 RPM, 5370 RPM, 4773 RPM, and 6260 RPM have been included in the Figure. For this combination of motor and controller, the peak acoustic radiation occurs at 4773 RPM near a frequency of 4500 Hz. The peak amplitudes of the tones produced at 4380 RPM are similar to those produced by the same motor and the E300 controller. The presence of additional discrete frequencies in the current signal not related to the fundamental line frequency (labeled f_a and f_b) produce tones at 4773 RPM, 5370 RPM and 6260 RPM. The analysis in Section III does not account for magnetic pressure associated with frequency components of the supply current that are not related to the fundamental line frequency. The peak acoustic radiation at 4773 RPM is close to that at 5370 RPM for the same motor and the E300 controller.

The results for the DJI 2312 motor and the sine wave controller are presented in Fig. 20. The peak amplitudes of the acoustic radiation near 5000 Hz are slightly higher for the E300 controller (see Fig. 18) than for the sine wave controller at 4380 and 5270 RPM. At 6260 RPM, the peak acoustic radiation is similar for both controllers.

Results for the DJI 2212 motor and motor loaded with a propeller are shown in Fig. 21. The data were acquired with the E300 controller. At 4380 RPM, motor tones are observed in the motor + propeller data at frequencies equal to $8*f_l$ and $10*f_l$. The differences in the amplitudes of these tones for the motor and motor + propeller data are roughly equal to the differences in the amplitudes of the corresponding 7th current harmonics (see Fig. 9) indicating these tones are associated with the rotor-stator interaction field as the rotor field does not increase with load (current), the stator field increases as the square of the current, and the rotor-stator interaction terms are proportional to the current coefficients (harmonics). Similarly, increases in amplitudes with loading for the $8*f_l$ tones at 5370 and 6260 RPM are

15

close to the increases in the corresponding 7th current harmonics. The amplitude of the tone at a frequency of $7*f_l$ for a motor speed of 5370 RPM is unaffected by loading indicating the tone is the result of a rotor-stator interaction term in Table 3 with $u = 4$ since the fourth harmonic of the supply current does not increase with load. The tone at a frequency of $7*f_l$ cannot be associated with the permanent magnet field as m and n in Table 3 are odd integers. The tones which increase with increasing current and are the result of an azimuthal mode 2 vibration of the rotor are associated with Term 6 in Table 3 (with $u = 7$) as the other terms will not result in a mode 2 loading of the rotor.

The results for the DJI 2212 motor and motor + propeller acquired with the sine wave controller are shown in Fig. 22. For 4380 RPM and 6260 RPM, no motor tones are observed in the motor + propeller data. For 4773 RPM, motor tones are observed in the motor + propeller data at the $8*f_l$ frequency. The amplitude is equivalent to that of the motor alone indicating the tone may be associated with the rotor magnetic field. At 5370 RPM, motor tones are observed in the motor + propeller data at $10*f_a$ with an amplitude slightly greater than that for the motor alone.

The results for the DJI 2312 motor alone and motor + propeller acquired with the E300 controller are shown in Fig. 23. For all motor speeds, the amplitudes of the motor tones occurring near the second vibration mode frequency are significantly greater than the broadband and propeller tones in the same frequency range. The amplitudes of the tones are at least 5 dB greater than those for the motor alone. Additionally, motor tones also appear in the motor + propeller data at frequencies near the first vibration mode at roughly 1200 Hz for a motor speed of 5370 RPM. At 6260 RPM, increases in acoustic radiation with loading occur around the $12*f_l$ frequency. Results for the DJI 2312 motor alone and motor + propeller with the sine wave controller are similar to those shown in Fig. 23 for the E300 controller.
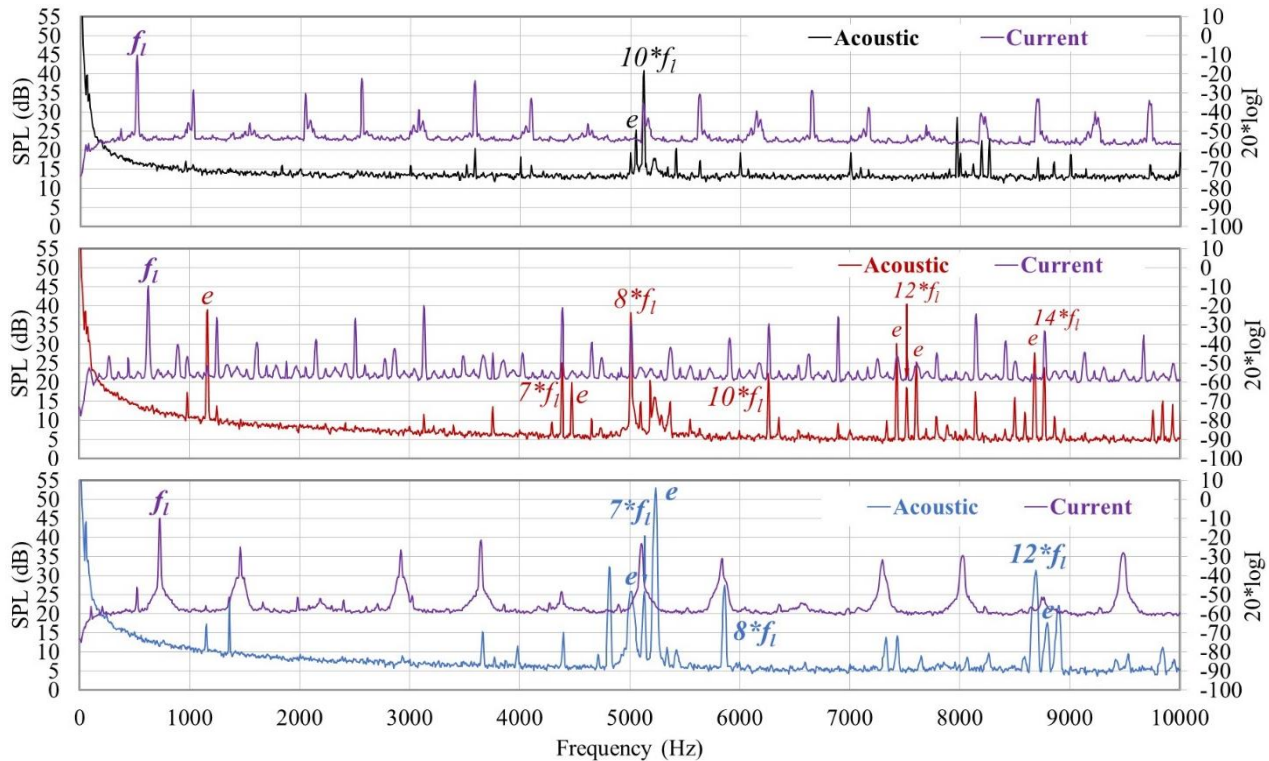
Figure 18. The acoustic data acquired for the DJI 2312 motor with the E300 controller. The data are for motor speeds equal to 4380 RPM (top), 5370 RPM (middle), and 6260 RPM (bottom). The eccentricity frequency, e, and harmonics of the fundamental line frequency, f_l, are marked for reference.
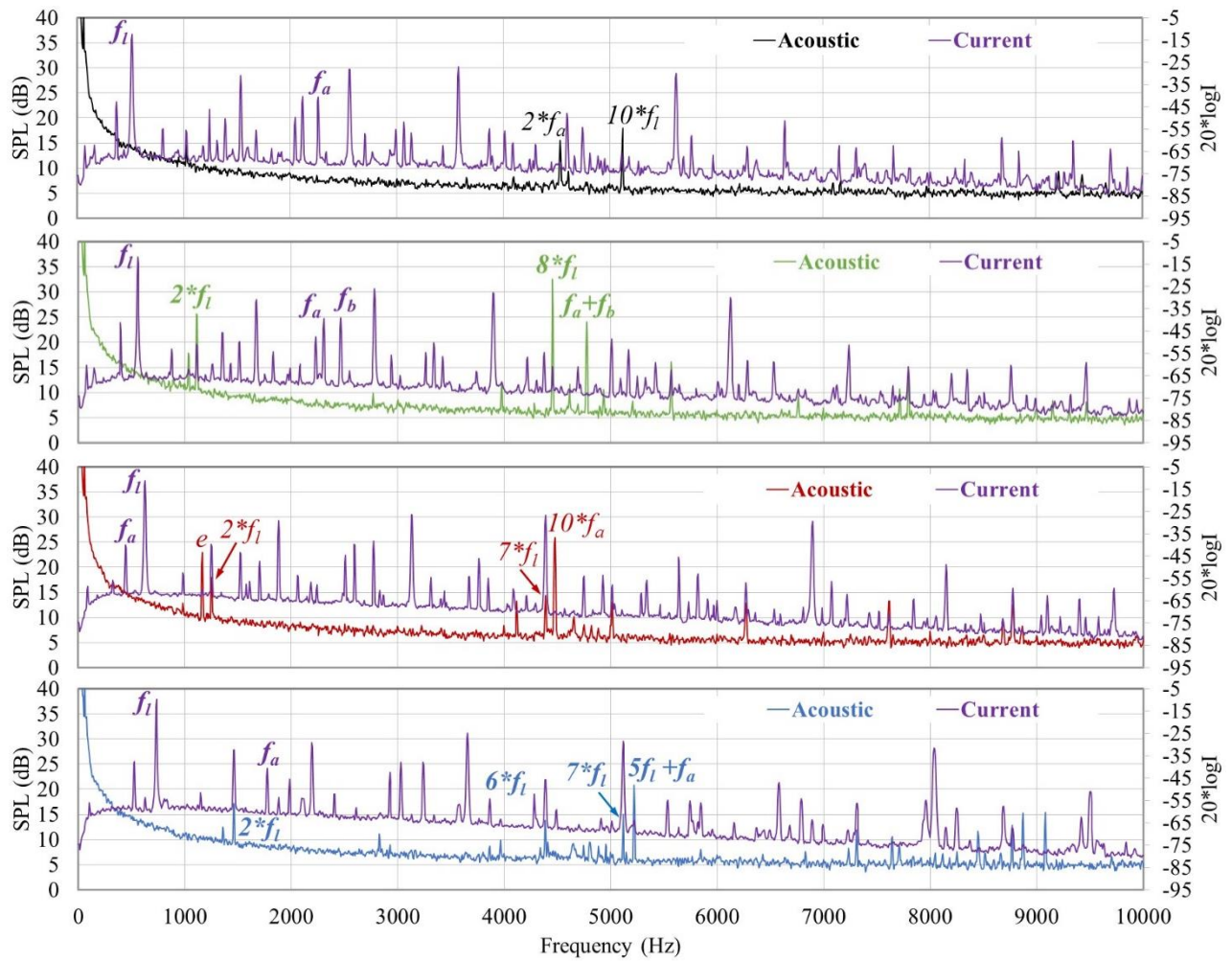
Figure 19. The acoustic data acquired with the DJI 2212 motor with the sine wave controller. The data are for motor speeds equal to 4380 RPM (top), 4773 RPM (row two), 5370 RPM (row 3), and 6260 RPM (bottom). The eccentricity frequency, e, the unexpected additional frequencies, f_a and f_b, and harmonics of the fundamental line frequency, f_l, are marked for reference.
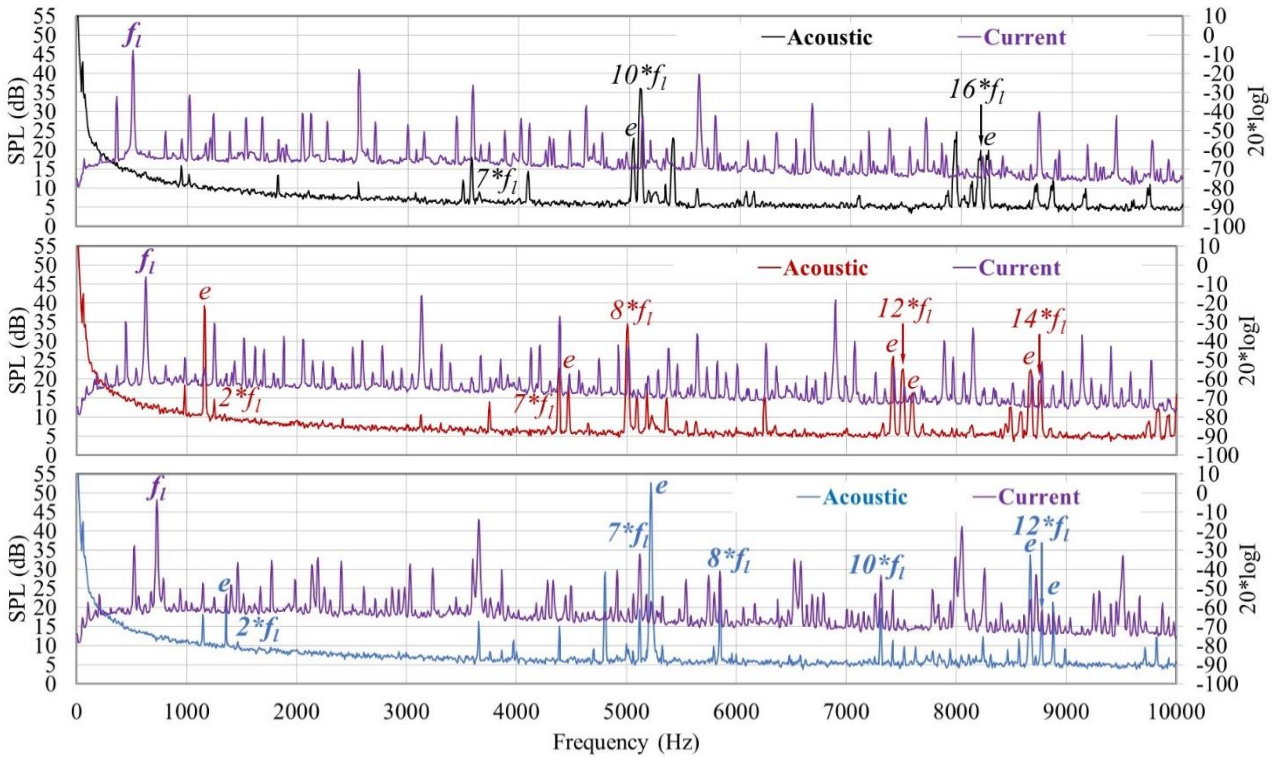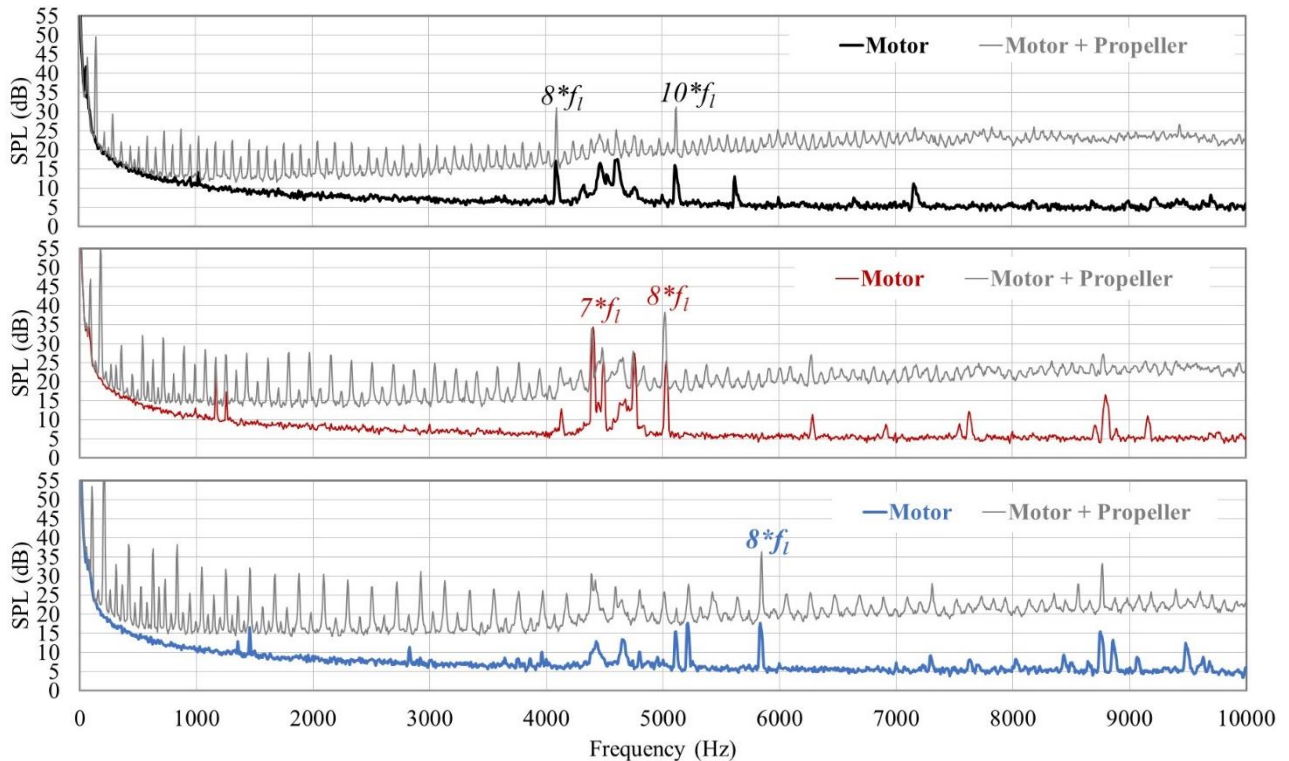
Figure 20. The acoustic data acquired for the DJI 2312 motor with the sine wave controller. The data are for motor speeds equal to 4380 RPM (top), 5370 RPM (middle), and 6260 RPM (bottom). The eccentricity frequency, *e*, and harmonics of the fundamental line frequency, f_l, are marked for reference.
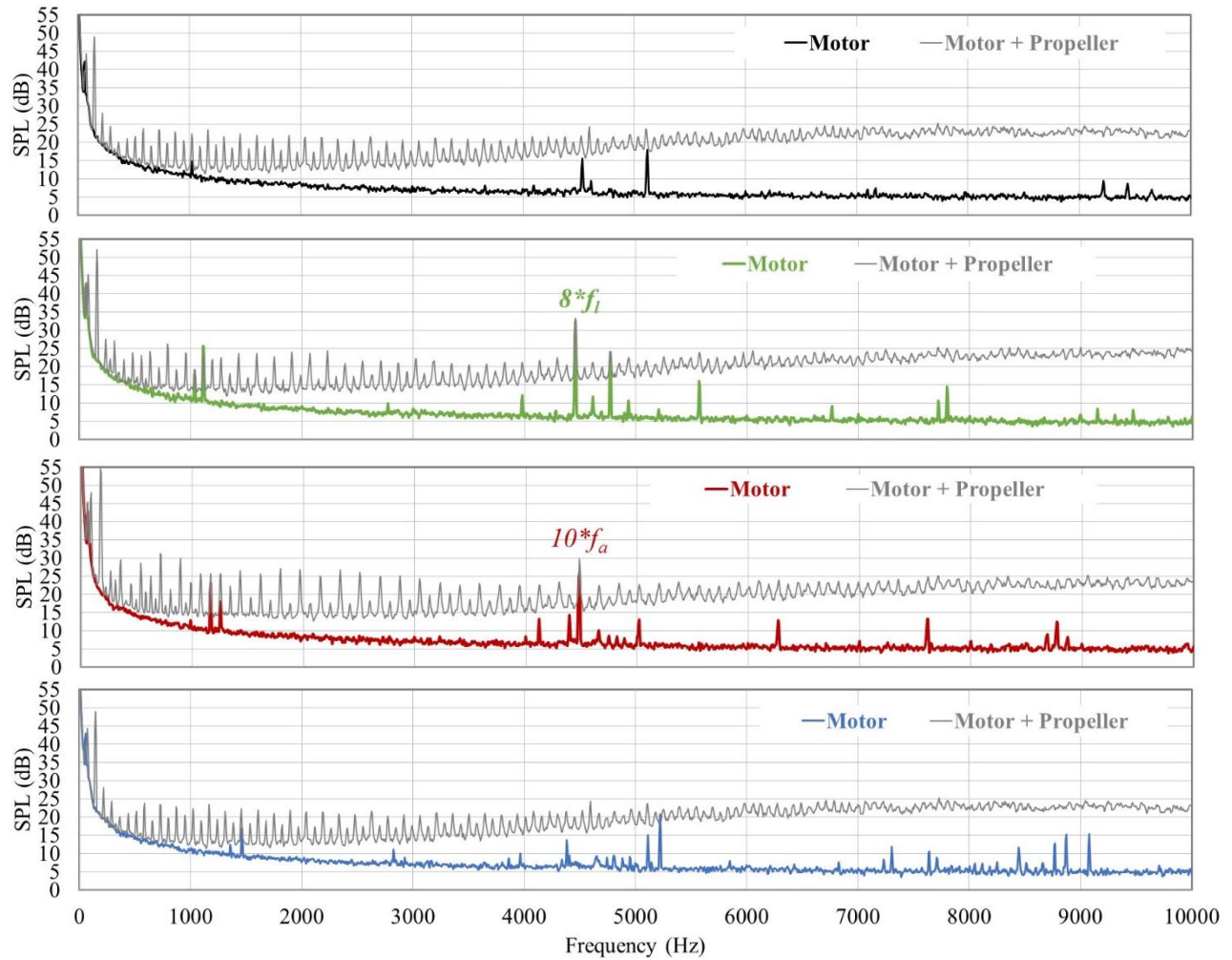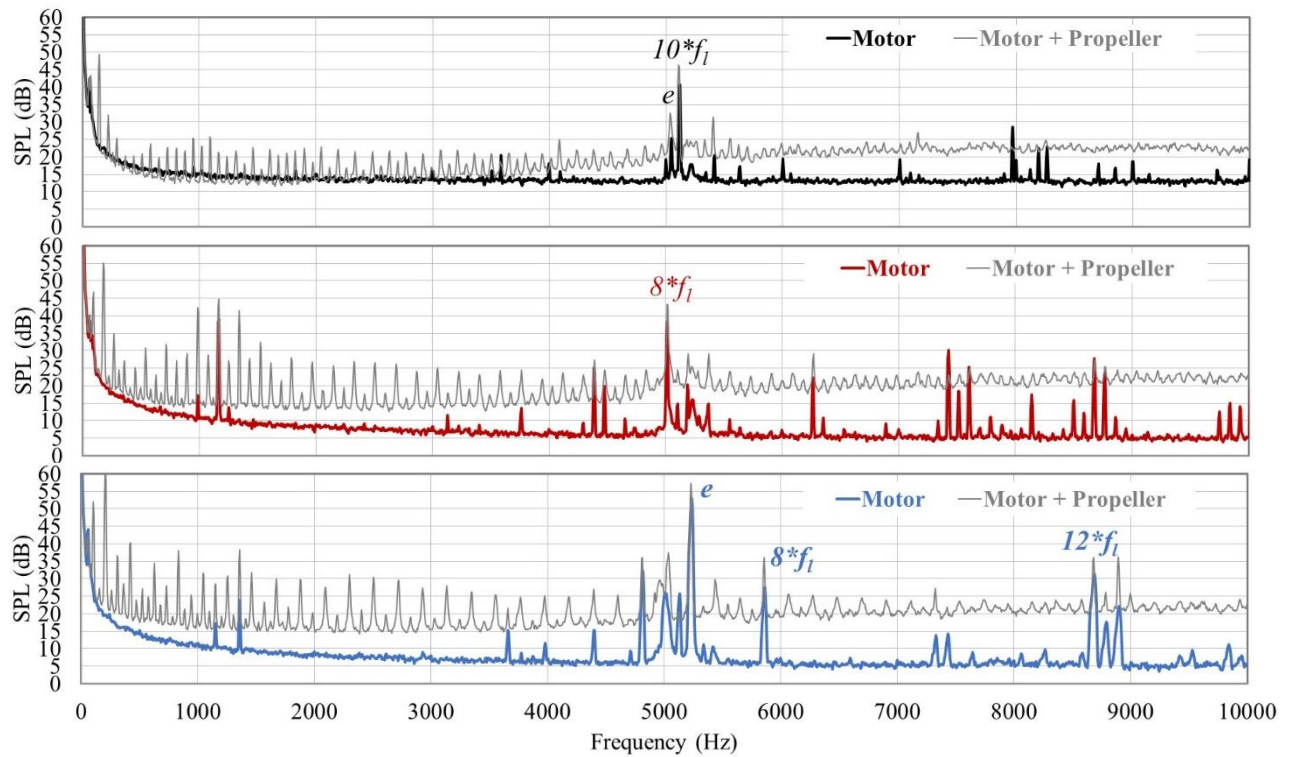

Figure 21. The acoustic data acquired for the DJI 2212 motor and motor loaded with a propeller. The data were acquired with the E300 controller and are for motor speeds equal to 4380 RPM (top), 5370 RPM (middle), and 6260 RPM (bottom). Harmonics of the fundamental line frequency, f_l, are marked for reference.

18

Figure 22. The acoustic data acquired for the DJI 2212 motor and motor loaded with a propeller. The data were acquired with the sine wave controller and are for motor speeds equal to 4380 RPM (top), 4773 (row 2) 5370 RPM (row 3), and 6260 RPM (bottom). Harmonics of the fundamental line frequency, f_l, and the unexpected additional frequency, f_a, are marked for reference.

Figure 23. The acoustic data acquired for the DJI 2312 motor and motor loaded with a propeller. The data were acquired with the E300 controller and are for motor speeds equal to 4380 RPM (top), 5370 RPM (middle), and 6260 RPM (bottom). The eccentricity frequency, e, and harmonics of the fundamental line frequency, f_l, are marked for reference.

D. Installed Acoustics

A comparison of the installed and uninstalled DJI 2212 motor with the E300 controller is shown in Fig. 24 for three operating speeds. The bandwidth for the data in the Figure is 12.2 Hz. The motor and controller are not the same samples as those used for the results in Fig. 16. The motor and controller combination used for the data in Fig. 24 produces fewer tones for the uninstalled motor at 4380 and 5370 RPM than that used for the data in Fig. 16. The uninstalled data in Fig. 24 show little evidence of acoustic radiation associated with the first rotor vibration mode around 1200 Hz and significant radiation at frequencies near 5000 Hz. The installed data show significant acoustic radiation at frequencies near the first rotor vibration mode and little or no increase (relative to the uninstalled motor) in the amplitudes of the tones near 5000 Hz for all motor speeds investigated. Additionally, the installed configuration results in broadband increases in acoustic radiation (relative to the uninstalled motor) over a range of frequencies between 2000 Hz and 4000 Hz.
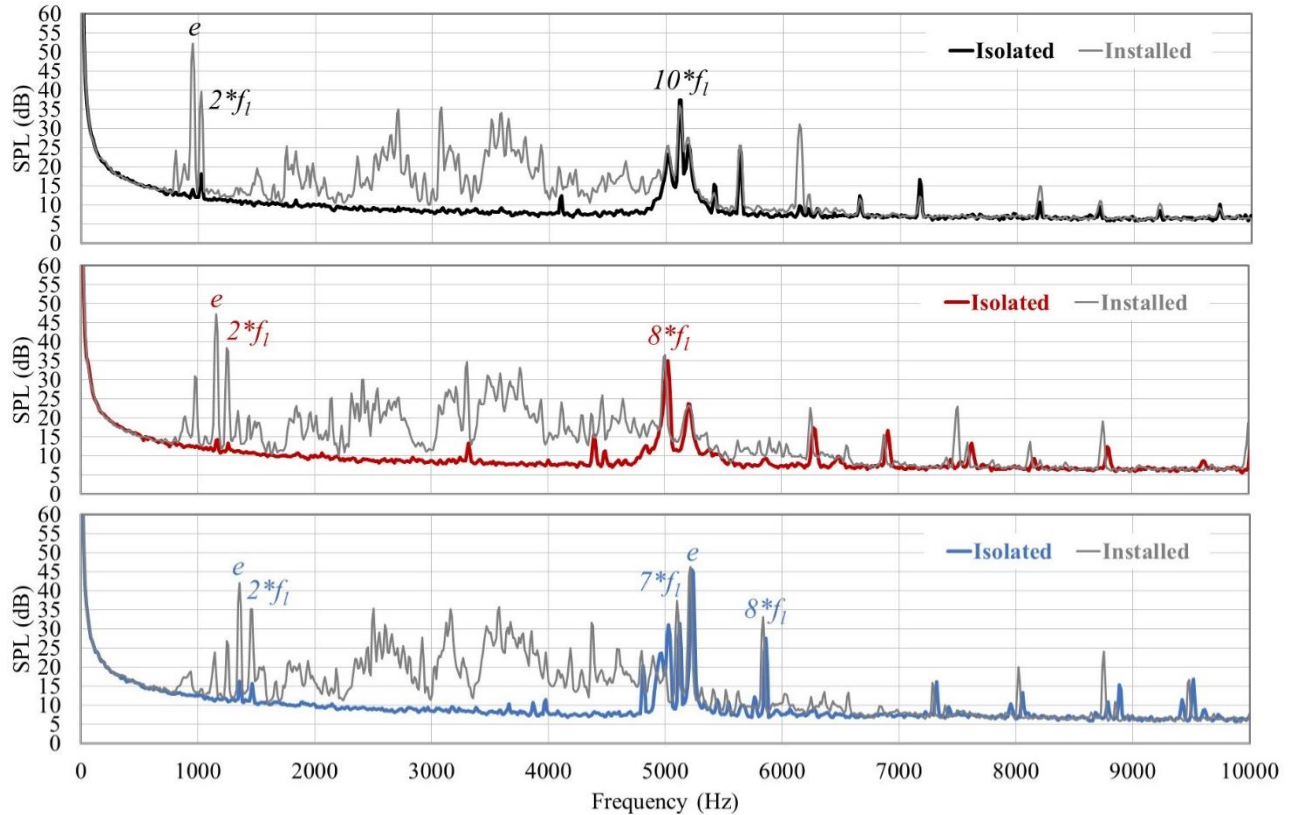
Figure 24. The acoustic data acquired for the DJI 2212 isolated and installed motor with the E300 controller. The data were acquired at 4380 RPM (top), 5370 RPM (middle), and 6260 RPM (bottom). Harmonics of the fundamental line frequency, f_l, are marked for reference.

V. Conclusions

Electromagnetic theory predicts electromagnetic pressure loading on the rotor at frequencies equal to integer multiples of the fundamental supply current line frequency. For pressure associated with the stator magnetic field or the rotor-stator interaction, increases in the supply current increase motor loading. Additionally, increased harmonic content in the current signal results in increased harmonic content of the pressure loading associated with the stator magnetic flux density. Increased harmonic content of the supply current increases the likelihood that the pressure loading frequency will be close to a resonance frequency of the motor.

The controllers used in the work reported here included sinewave and conventional controllers. For all controllers, the pulse-width modulation frequency was greater than 15 kHz and, therefore, did not contribute to the acoustic radiation in the frequency range of interest. Both types of controllers produced supply currents that exhibited significant frequency content. For some motor speeds, frequencies not related to the fundamental line frequency were observed in the supply current data. For the DJI controllers, more tones were present in the current probe measurements for the sine wave controller than for the conventional controller.

Vibration measurements for an open-circuit (static) motor indicated all motors had mode 2 vibration frequencies in the range of 4400 – 5100 Hz. Finite element analysis showed a mode 1 vibration frequency for the DJI 2212 motor equal to roughly 1200 Hz. Resonance frequencies were slightly altered with rotation. Measured vibration amplitudes for mode 1 and 2 were 5 μm and 0.5 μm, respectively, for an unloaded motor.

Acoustic measurements showed peak acoustic levels were a function of motor, controller, and motor speed. For all configurations and conditions investigated, tones were produced in the 4500 – 5500 Hz range, a frequency range which includes the frequencies associated with the azimuthal mode 2 vibration of the motor rotors. For limited configurations and speeds, acoustic radiation was observed at frequencies associated with the mode 1 vibration. The largest acoustic amplitudes occurred for the DJI 2312 motor at the highest motor speed investigated and were associated with motor dynamic eccentricity. The frequency content of the sine wave controllers resulted in acoustic radiation at frequencies other than integer multiples of the fundamental line frequency for some configurations and conditions. Acoustic measurements conducted with a motor loaded with a propeller showed that electric motor tones were observed in the spectra for a range of motors, controllers, and speeds with frequencies near those of the azimuthal mode 2 vibration frequency and, for some configurations and speeds, at frequencies near the azimuthal mode 1 vibration frequency.

Installed motor measurements showed that acoustic radiation at frequencies near the azimuthal mode 1 vibration frequency were elevated by installation in a quadcopter body. Additionally, installation was found to increase acoustic levels over a range of frequencies between 2000 Hz and 4000 Hz. Acoustic radiation near the azimuthal mode 2 vibration frequency was not impacted by installation.

References

[1]Amazon Prime Air, https://www.amazon.com/Amazon-Prime-Air/b?node=8037720011

[2]Holden, J and Goel, N., "Fast-Forwarding to a Future of On-Demand Urban Air Transportation," UBER Elevate Summit, October 27, 2016. https://www.uber.com/info/elevate/

[3]Huff, D. and Henderson, B. "Electric Motor Noise from Small Quadcopters: Part I – Acoustic Measurements," 28th AIAA/CEAS Aeroacoustics Conference, 2018.

[4]Gieras, J. F., Wang, C., and Lai, J. C., *Noise of Polyphase Electric Motors*, CRC Press, 2006, pp. 47, 110 – 113

[5]Gieras, J. F., Wang, C., Joseph, C. S. L., and Ertugrul, N., "Analytical Prediction of Noise of Magnetic Origin Produced by Permanent Magnet Brushless Motors," Electric Machines & Drives Conference, 2007. IEMDC '07. IEEE International

[6]Zhu, Z. Q., Howe, D., Bolte, E., and Ackermann, B., "Instantaneous Magnet Field Distribution in Brushless Permanent Magnet dc Motors, Part I: Open-Circuit Field," IEEE Transactions on Magnetics 29 [1], 1993, pp. 124 – 135.

[7]Zhu, Z. Q. and Howe, D., "Instantaneous Magnet Field Distribution in Brushless Permanent Magnet dc Motors, Part II: Armature Reaction Field," IEEE Transactions on Magnetics 29 [1], 1993, pp. 136 – 142.

[8]Zhu, Z. Q. and Howe, D., "Instantaneous Magnet Field Distribution in Brushless Permanent Magnet dc Motors, Part III: Effect of Stator Slotting," IEEE Transactions on Magnetics 29 [1], 1993, pp. 143 – 151.

[9]Zhu, Z. Q. and Howe, D., "Instantaneous Magnet Field Distribution in Brushless Permanent Magnet dc Motors, Part IV: Magnetic Field," IEEE Transactions on Magnetics 29 [1], 1993, pp. 152 – 158.

[10]Huang, S., Aydin, M., and Lipo, T. A. "Electromagnetic Vibration and Noise Assessment of Surface Mounted PM Machines," Power Engineering Society Summer Meeting, IEEE, 2001.

[11]Kim, U. and Lieu, D. K. "Effects of Magnetically Induced Vibration Force in Brushless Permanent-Magnet Motors," IEEE Trans. On Magnetics, 2005, Vol. 41, No. 6, pp. 2164 – 2172.

[12]Rezig, A., Mekideche, M. R., and Djerdir, A. "Effect of Rotor Eccentricity Faults on Noise Generation in Permanent Magnet Synchronous Motors," Progress in Electromagnetics Research C, 2010, Vol. 15, pp. 117 - 132.

[13]Yu, S. and Tang, R. "Electromagnetic and Mechanical Characterization of Noise and Vibration in Permanent Magnet Synchronous Machines," IEEE Trans. Of Magnetics, 2006, Vol. 42, No. 4, pp. 1335 – 1338.

[14]Starschich, E., Muetze, A., and Hameyer, K. "Analytical Force Calculation in Brushless-DC Motors I: An Alternative Approach," Electric Machines and Drives Conference, 2009. IEMDC '09. IEEE International.

[15]Behbahanifard, H. and Sadoughi, A. "Cogging Torque Reduction in Line Start Permanent Magnet Synchronous Motor," J. Electr. Eng. Technol. 2016, 11 no. 4, pp. 709 – 718.

[16]Deodhar, R. P., Staton, D. A., Jahns, T. M., and Miller, T. J. E. "Prediction of Cogging Torque Using the Flux-MMF Diagram Technique," IEEE Transaction on Industry Applications, 32 no. 3, 1996, pp. 569 – 576.

[17]Erdelyi, E. and Horvay, G. "Vibration Modes of Stators of Induction Motors," J. Applied Mechanics, 1957, 23 (Transactions of ASME, Vol. 78), pp. 30 – 45.

[18]Ellison, A. J. and Yang, S. J. "Natural Frequencies of Stators of Small Electric Machines," Proc. IEE, 1971, 118 mo. 1, pp. 185 – 190.

[19]Castano, S., Bilgrin, B., Lin, J., and Emadi, A. "Radial Forces and Vibration Analysis in an External-Rotor Switched Reluctance Machine, IET Electric Power Applications, 2017, 11 no. 2, pp. 252 – 259.

[20]Liu, G., Qiu, G., Qiu, F., and Cao, Wenping. "Outer Rotor Mechanical and Dynamical Performance Analysis for High-Speed Machine," 2016 IEEE Transportation Electrification Conf. and Expo, Asia-Pacific (ITEC), Busan, Korea.

[21]Huang, S.-C. and Soedel, W., "On the Forced Vibration of Simply Supported Rotating Cylindrical Shells," J. Acoust. Soc. Am. 84, 1988, pp. 275 – 285.

[22]Mikulas, M. M. and McElman, J. A. "On Free Vibrations of Eccentrically Stiffened Cylindrical Shells and Flat Plates," NASA TN D-3010, 1965.

[23]Crocker M. J. and Kessler, F. M., *Noise and Noise Control*, Vol. II, CRC Press, 1982, p. 77.

[24]Ellison, A. J. and Yang, S. J. "Calculation of Acoustic Power Radiated by an Electric Machine," Acustica, 25, 1971, pp. 28 – 34.

[25]Erdelyi, E. "Predetermination of Sound Pressure Levels of Magnetic Noise of Polyphase Induction Motors," 1955, pp. 1269 – 1280.

[26]Yang, S. J. "Effect of Length-Diameter Ration on Noise Radiation from Electrical Machine," Acustica, 1975, 32, pp. 255 – 261.

[27]Yang, S. J. "On the Calculation of Acoustic Power Radiated by an Electrical Machine, International Conference on Electrical Machines and Drives, 1987, pp. 118 – 125.